Draft version August 31, 2021
Typeset using LaTeX **twocolumn** style in AASTeX631

Radio Emissions in Infrared Dark Clouds: Molecular Transitions and Continuum Maps

Dylan Gayer[1] and Pedro Beaklini[2]

[1] *Coe College, 1220 First Avenue NE, Cedar Rapids, IA 52402*
[2] *National Radio Astronomy Observatory, 1003 Lopezville Road, Socorro, NM 87801*

ABSTRACT

Since the beginning of ALMA's operation, we have access to new information about the birth of massive stars. Many projects and surveys that have been performed focus on the study of infrared dark clouds, identified as IRDC. These sources are composed of many cores of dust condensations and low-temperature dense gas. This project uses the ALMA and VLA data archive to search for similarities between the various sources, in the continuum maps and, in some cases, the molecular line emissions. We have found three sources, IRDC-B1, IRDC-B2, and IRDC-C9, that show molecular line emissions of sulfur-bearing molecules, and in the case of IRDC-B2 and IRDC-C9, complex organic molecules.

1. INTRODUCTION

There are many efforts by the community to answer the numerous questions regarding the formation of massive stars. There are two main models for massive star formation: the turbulent core accretion model and the competitive accretion model. The turbulent core accretion model states that turbulence and magnetic fields regulate the fragmentation of the star forming clumps that cannot be supported by thermal pressure alone, to form cores with initial conditions set by the environmental pressure with the accretion rate defined by the free fall time (McKee et al. 2003; Tan et al. 2013). In essence, the turbulent core accretion model shows that massive protostars are formed by the initial collapse of the molecular cloud, bringing in enough mass to form a massive protostar. The competitive accretion model states that for a molecular cloud with many pre-main sequence stars, the stars nearer to the cloud center accrete non-gravitationally bound gas at a faster rate than those at a distance further from the cloud center (Bonnell et al. 1997; Bonnell et al. 2001). In other words, the competitive accretion model states that even after forming low-mass protostars, these protostars compete with each other for the non-gravitationally bound gas in the region, and thus the protostars at the lowest gravitational potential accrete more gas and grow to massive protostars.

Following these two main models for massive star formation, a region that is a birth place for massive stars (de Wit et al. 2005; Battersby et al. 2014) is an InfraRed Dark Cloud (IRDC). IRDCs are low-temperature, dense condensations of gas and dust that are optically thick when compared to the Galactic infrared background emission (Butler et al. 2009). Since these regions are a birth place for massive stars (de Wit et al. 2005; Battersby et al. 2014), these models should hold for massive starless cores in IRDCs.

2. OBJECTIVES

Since the construction of Atacama Large Millimeter Array (ALMA), we have gained important information about massive star formation and molecular clouds. The main objective for this project was to further study ALMA and Karl G. Jansky Very Large Array (VLA) archive data in hopes of learning more about these molecular clouds and early massive star formation. We used the work of four surveys from the archives to help us study sources in IRDCs through the analysis of continuum maps and study of molecular emissions: ALMA Surveys:

- Kong et al. 2017 - N_2D^+ Line Emission in IRDCs
- Li et al. 2020 - CO and SiO Outflows in IRDCs
- Liu et al. 2021 - SiO Outflows in IRDCs

VLA Surveys:

- Liu et al. 2021 - C-Band Observations in IRDCs
- Purser et al. 2021 - Radio Jets in Massive Young Stellar Objects (MYSOs) and IRDCs

3. OBSERVATIONS

3.1. *Archive Data*

The IRDC survey by Kong et al. (2017) focused on finding the N_2D^+(3-2) line emission in IRDCs as a signature for a massive starless core on the verge of collapse. The existence of massive starless cores would favor the turbulent core accretion model over the competitive accretion model. Furthermore, the works of Li et al. (2020) studied CO and SiO outflows and Liu et al. (2021) studied CO outflows from a subset of and all of the cores identified by Kong et al. (2017), respectively. Since it is known that one of the sources has prominent line emissions (as shown in Beaklini et al. 2020), there is reason to search other sources for line emissions as well. This work searches other clumps located in the IRDCs observed in the work by Kong et al. (2017) to identify other sources with prominent line emissions.

The survey identifying massive starless cores (Project Code: 2013.1.00806.S, PI: J. Tan) as reported by Kong et al. (2017) was carried out with ALMA band 6 (211-275 GHz), with the 12 m array in the most compact configuration during observation cycle 2. These cores were identified by searching for the N_2D^+ emission in 32 IRDCs. More information on the observations can be found in Kong et al. (2017).

This data was split into four basebands: baseband 1 has a single spectral window centered at 231.32 GHz to capture N_2D^+(3-2) transitions, baseband 2 has a single spectral window used for a continuum observation centered on 231.00 GHz with a large bandwidth of 1.87 GHz and a large channel width of about 974 KHz, baseband 3 has a single spectral window centered at 219.56 GHz to capture $C^{18}O$(2-1) transitions, and baseband 4 has four spectral windows centered at 216.11 GHz to capture DCO^+(3-2) transitions, 216.95 GHz to capture CH_3OH transitions, 217.20 GHz to capture SiO(5-4) transitions, and 217.24 GHz to capture DCN(3-2) transitions. We performed the data analysis using CASA (Common Astronomy Software Application) in baseband 2, to search for additional molecular lines.

The survey by Purser et al. (2021) was performed using Q-band (44 GHz) observations in the A configuration (2014-2015, Project Codes: 14A-141 and 15A-238, PIs: S.L. Lumsden and S.J.D. Purser, respectively). The A configuration data set has a bandwidth of 8 GHz with 64 SPWs of 64 × 2 MHz channels with 3-bit samplers and a velocity resolution of 12 km/s. Since the velocity resolution is not enough to resolve lines with a FWHM of 2.2 km/s (Beaklini et al. 2020), we use the continuum data to observe the clumps with the higher spatial resolution of this data than the ALMA data above.

3.2. *Data Cleaning*

We calibrated the data presented in Kong et al. (2017) using standard pipeline calibration procedures. After calibration, we cleaned the image using the standard Hogbom algorithm and Briggs weighting (with the Briggs robustness parameter set to zero) over 1000 iterations. The result was a 768 × 768 pixel image with 0.08 arcsec cell size. The final continuum band image was obtained after performing self-calibration with the Multi-term Multi Frequency Synthesis (MTMFS) algorithm and Briggs weighting (with the Briggs robustness parameter set to zero) over 1000 iterations beginning with phase calibration cycles and ending with a single amplitude calibration cycle. Typically, only two cycles were needed to get sufficient noise reduction. The same self-calibration procedure was also applied to the ALMA data cube with 1920 channels.

Since the original data of the project was divided into two tracks, we focused on the track containing sources A, B, C, and E (following the nomenclature of Butler et al. 2012), as the IRDC-C9 complex has a prominent source with line emission features as discussed in Beaklini et al. (2020).

4. RESULTS

The continuum images for sources A1, A2, A3, B1, B2, C2, C3, C4, C5, C6, C7, C8, C9, E1, and E2 are shown in Figure 1 where the surface brightness temperature has units of Jy/beam. In many of the continuum maps, we can clearly see the presence of compact substructures associated with these sources (referred to as 'clump,' where the brightness is denoted as bright if the clump has a central brightness greater than 0.3 σ). In the following subsections, we briefly discuss the structures and spectral emissions of these sources.

4.1. *IRDC-A1*

IRDC-A1 consists of a single bright clump with a flux density of 1.748e-02 mJy/beam.

The emission spectrum for the bright clump in IRDC-A1 does not clearly show potential lines and has an average noise level of around 0.08 K.

4.2. *IRDC-A2*

IRDC-A2 consists of a single bright clump that is surrounded by many dim clumps. The bright clump has a flux density of 4.019e-03 mJy/beam.

The emission spectrum for the bright clump in IRDC-A2 does not clearly show potential lines and has an average noise level of around 0.6 K.

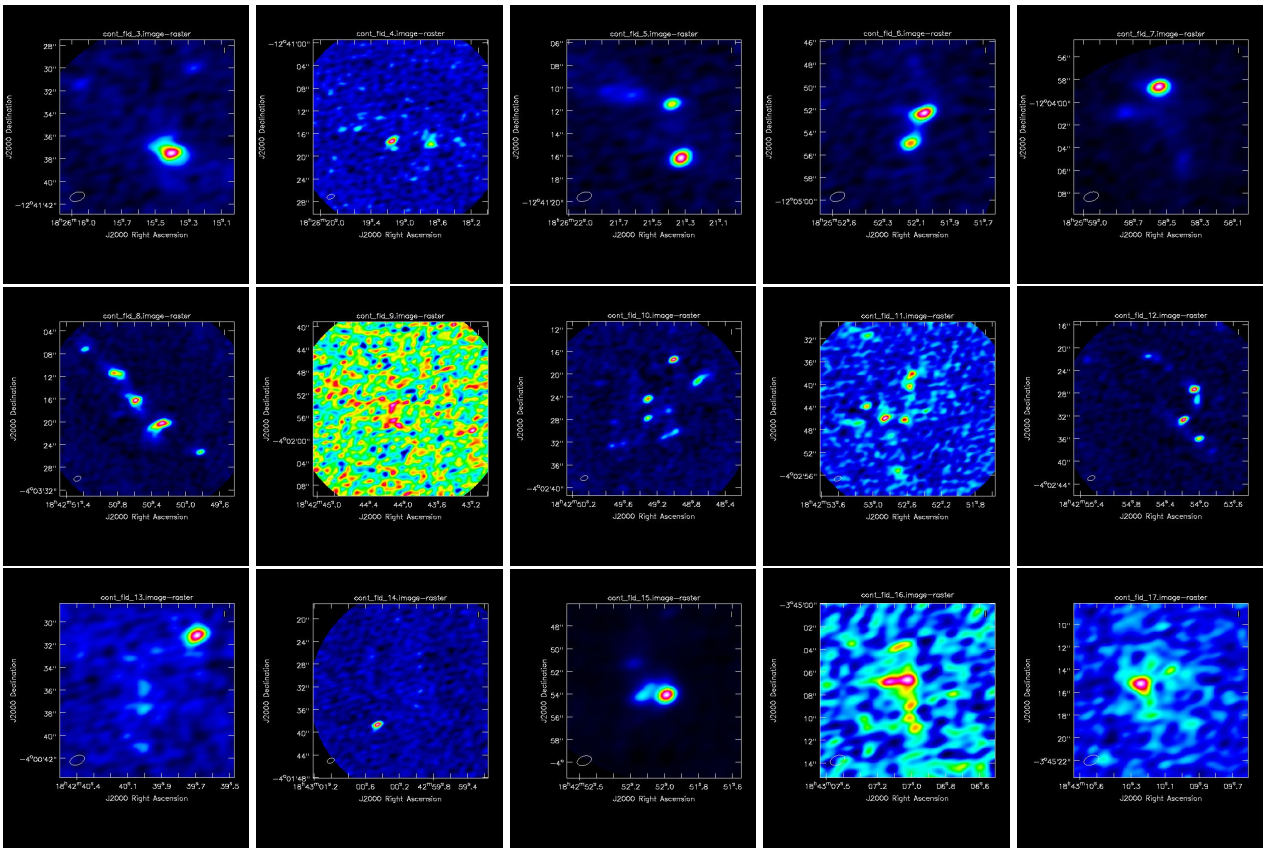

Figure 1. Continuum Maps for the IRDCs identified in Kong et al. (2017) where the color gradient goes from dark blue to bright red, where the lowest value in the continuum map is represented by dark blue and the greatest value is represented by bright red. Starting from the left, the top row contains sources IRDC-A1, IRDC-A2, IRDC-A3, IRDC-B1, and IRDC-B2. The middle row contains sources IRDC-C2, IRDC-C3, IRDC-C4, IRDC-C5, IRDC-C6. The bottom row contains sources IRDC-C7, IRDC-C8, IRDC-C9, IRDC-E1, and IRDC-E2.

4.3. *IRDC-A3*

IRDC-A3 consists of a bright clump with a nearby dim clump. The bright clump has a flux density of 1.299e-02 mJy/beam.

The emission spectrum for the bright clump in IRDC-A3 does not clearly show potential lines and has an average noise level of around 0.13 K.

4.4. *IRDC-B1*

IRDC-B1 has two bright clumps where the top clump is brighter than the bottom clump. The top clump has a flux density of 1.415e-02 mJy/beam.

IRDC-B1 does show a marginal detection of the OCS(19-18) transition, which will be discussed further in the next section, and has an average noise level of around 0.05 K.

4.5. *IRDC-B2*

IRDC-B2 has a bright clump surrounded by two main dim clumps. The bright clump has a flux density of 2.306e-02 mJy/beam.

IRDC-B2 shows a detection of the OCS(19-18), ^{13}CS(5-4), and Methanol transitions, along with many other Complex Organic Molecules (COMs) and these lines will be discussed further in the next section. This clump has an average noise level of around 0.06 K.

4.6. *IRDC-C2*

IRDC-C2 has two bright clumps with three dim clumps in a line. The bottom, larger bright clump has a flux density of 3.868e-02 mJy/beam.

The emission spectrum for the bottom, larger bright clump in IRDC-C2 does not clearly show potential lines and has an average noise level of around 0.14 K.

4.7. *IRDC-C3*

IRDC-C3 has too much noise to confidently identify structures.

Since we could not confidently identify structures, there was no clear region to inspect molecular emissions in IRDC-C3.

4.8. *IRDC-C4*

IRDC-C4 has two bright clumps and many dim clumps. The top right, larger bright clump has a flux density of 6.767e-03 mJy/beam.

The emission spectrum for the top right, larger bright clump in IRDC-C4 does not clearly show potential lines and has an average noise level of around 0.12 K.

4.9. *IRDC-C5*

IRDC-C5 has five bright clumps and many dim clumps. The bottom center, largest bright clump has a flux density of 2.994e-03 mJy/beam.

The emission spectrum for the bottom center, largest bright clump in IRDC-C5 does not clearly show potential lines and has an average noise level of around 0.07 K.

4.10. *IRDC-C6*

IRDC-C6 has two bright clumps and three dim clumps. The upper, brighter clump has a flux density of 1.065e-02 mJy/beam.

The emission spectrum for the upper bright clump in IRDC-C6 does not clearly show potential lines and has an average noise level of around 0.11 K.

4.11. *IRDC-C7*

IRDC-C7 has a bright clump and ten dim clumps. The bright clump has a flux density of 5.321e-03 mJy/beam.

The emission spectrum for the bright clump in IRDC-C7 does not clearly show potential lines and has an average noise level of around 0.09 K.

4.12. *IRDC-C8*

IRDC-C8 has a bright clump and six dim clumps. The bright clump has a flux density of 3.517e-03 mJy/beam.

The emission spectrum for the bright clump in IRDC-C8 does not clearly show potential lines and has an average noise level of around 0.09 K.

4.13. *IRDC-C9*

IRDC-C9 has a bright clump and two dim clumps. The bright clump has a flux density of 1.557e-01 mJy/beam.

As reported in Beaklini et al. (2020) and shown in Figure 2, the bright clump in IRDC-C9 shows a detection of OCS(19-18), ^{13}CS(5-4), and Methanol, along with many other Complex Organic Molecules (COMs) which will be discussed further in the next section. This bright clump has an average noise level of .013 K.

4.14. *IRDC-E1*

IRDC-E1 has six bright clumps and many dim clumps. The largest bright clump has a flux density of 4.079e-03 mJy/beam.

The emission spectrum for the bright clump in IRDC-E1 does not clearly show potential lines and has an average noise level of around 0.05 K.

4.15. *IRDC-E2*

IRDC-E2 has a bright clump surrounded by many dim clumps. The bright clump has a flux density of 4.487e-03 mJy/beam.

The emission spectrum for the bright clump in IRDC-E2 does not clearly show potential lines and has an average noise level of around 0.08 K.

5. DISCUSSION

Figure 2 shows the emission spectra of IRDC-C9, IRDC-B2, and IRDC-B1; although the emissions of IRDC-B2 and IRDC-B1 are about five times more faint than those of IRDC-C9, we have found peaks at frequencies corresponding to those in IRDC-C9 that have been published in Beaklini et al. (2020). Through comparison with the lines identified by Beaklini et al. (2020), we have identified the OCS(19-18), ^{13}CS(5-4), CH_3OH(10-9), $HCOOCH_3(20_{9,11}\text{-}20_{8,12})$, and $CH_3CH_2CN(27_{0,27}\text{-}26_{0,26})$ transitions in IRDC-B2, as well as the unidentified peak at 232.411 GHz. Due to IRDC-B1 having a marginal detection of a peak at 231.02 GHz and being located in the same IRDC as IRDC-B2, we find this to be the OCS(19-18) transition line. An additional finding is a difference in the ratios of the intensities of the peaks in IRDC-C9 and IRDC-B2. The ratio between the intensities of the OCS and ^{13}CS emission lines is 1.266 and 1.066 for IRDC-C9 and IRDC-B2, respectively. The ratio between the intensities of the ^{13}CS and CH_3OH emission lines is 1.148 and 2.566 for IRDC-C9 and IRDC-B2, respectively. The ratio between the intensities of the $HCOOCH_3(20_{9,11}\text{-}20_{8,12})$ and $CH_3CH_2CN(27_{0,27}\text{-}26_{0,26})$ emission lines is 0.487 and 0.609 for IRDC-C9 and IRDC-B2, respectively. The ratio between the intensities of the $CH_3CH_2CN(27_{0,27}\text{-}26_{0,26})$ and the unidentified peak at 232.411 GHz emission lines is 1.093 and 1.155 for IRDC-C9 and IRDC-B2, respectively. A difference in the chemical composition or, the more likely option, a difference in temperature of the clumps can explain these differences in the ratios between the intensities of the lines. The reason a difference in temperature is more likely is due to the fact that as the temperature of the clump increases, more molecules sublimate from the ice, increasing their col-

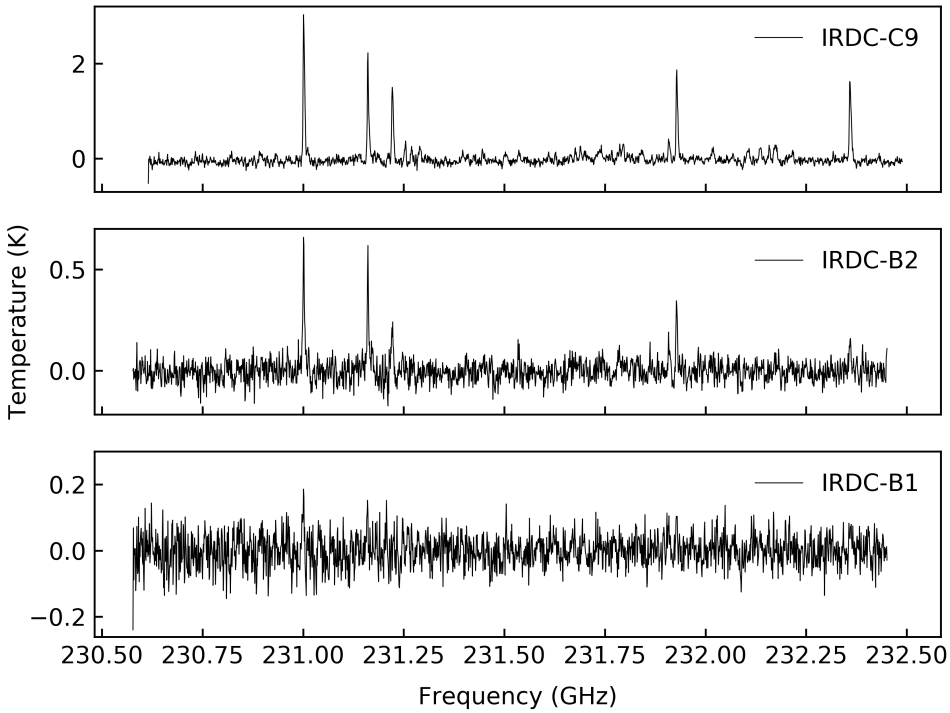

Figure 2. IRDC-C9 Continuum Subtracted Emission Spectrum (Top), IRDC-B2 Continuum Subtracted Emission Spectrum (Middle), and IRDC-B1 Continuum Subtracted Emission Spectrum (Bottom).

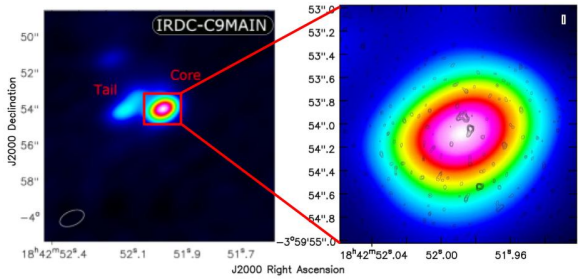

Figure 3. Left: Continuum image of IRDC-C9 from Beaklini et al. (2020). Right: VLA Contours (0.3, 0.4, 0.5, 0.6, 0.7, 0.8)σ over ALMA self-calibrated continuum image where the colors range from 0 to 0.07 Jy/beam.

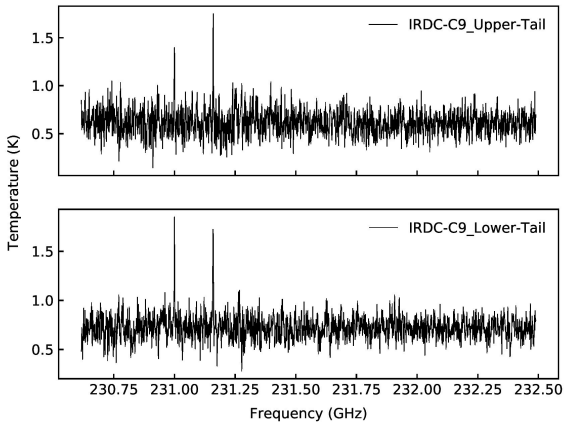

Figure 4. IRDC-C9 Upper Tail emission spectrum (Top), IRDC-C9 Lower Tail emission spectrum (Bottom).

umn densities, and thus, the brightness of the molecular lines.

In regards to IRDC-C9, there are more findings. The work by Beaklini et al. (2020) reports the sulfur-bearing molecules, OCS and ^{13}CS, having intensities that correspond to a temperature around 25K, while $^{13}CH_3CN$ has a rotational diagram corresponding to a temperature around 450K. The two smaller clumps identified within the bright clump of IRDC-C9 in the VLA contours shown in Figure 3 could explain the difference in temperatures if they have different temperatures or chemical compositions. Future work will try to constrain the temperatures and chemical compositions of these clumps.

Furthermore, Beaklini et al. (2020) discusses the emissions from two clumps, the core and the tail, in IRDC-C9; however, Liu et al. (2020) identifies two small clumps within the tail, but does not report spec-

tral emissions. We have investigated the emissions of the two small clumps within the tail of IRDC-C9 and found different emissions within each, as shown in Figure 4. Both the upper and lower components of the tail show detections of the OCS(19-18) and ^{13}CS(5-4) transitions; however, we do not find the marginal detections of the $HCOOCH_3(20_{9,12}\text{-}20_{8,13})$ and $CH_3CH_2CN(27_{0,27}\text{-}26_{0,26})$ emission lines as reported in Beaklini et al. 2020. Further differences arise when comparing the ratio between the intensities of these peaks: 0.789 and 1.072 for the upper and lower components, respectively. Similarly to the comparison between IRDC-C9 and IRDC-B2, there is likely a difference in the temperatures of these clumps.

What we believe we are seeing throughout this work is that these clumps are at different stages of stellar birth.

6. VLA PROPOSAL

We have submitted a proposal for VLA time using the Q-band in A configuration following the observation reported in Purser et al. (2021) to get data on IRDC-C9 with a higher velocity resolution (1.2 km/s). We are looking for the lower transitions of the OCS, ^{13}CS, and SiO lines previously detected in IRDC-C9 by Beaklini et al. (2020) and Liu et al. (2021). Since CS is more abundant than ^{13}CS, we have decided to instead look for the CS transition. The reason for looking at the low transitions of SiO is because SiO is an outflow tracer in which the SiO(5-4) outflow has been detected in Li et al. (2020) and Liu et al. (2021). Using the 8-bit correlator, we have requested the use of 8 subbands in both basebands where 3 subbands have 640 channels and are set aside to study the emission lines CS(1-0) at 48.9910 GHz, OCS(4-3) at 48.6516 GHz, and SiO(1-0) at 43.4238, while the remaining 13 subbands have 64 channels and are used to detect the continuum emission. From our observation setup, we have requested a continuum image with 15μJy of rms noise, achieving a signal/noise ratio almost 4 times higher than the current VLA data on the archive.

In addition to the IRDC-C9 observation, we requested continuum emission data from IRDC-B1 and IRDC-B2 using the 3-bit correlator with 8 GHz of bandwidth centered at 45 GHz to try and detect the low transitions of OCS and CS as well as search for other transitions in these sources. We have requested a continuum image with 20μJy of rms noise to resolve the structures of each source.

7. FUTURE WORK

In the future, we plan on working towards identifying the remaining peaks (e.g. the COMs at higher frequencies in Figure 2 Middle) in the B2 line emission data, predicting possible mass and temperature values for the clumps, gathering more data from the archives, and classifying the continuum maps for structures in order to find relations between sources.

We will also try to fit the grey body equation to the continuum flux detected in each clump. The grey body equation (Preibisch et al. 1993 and Elia et al. 2010) fits the sub-mm emission depending on its temperature and mass, following the equation below,

$$S_\nu = \frac{M\kappa_0}{d^2}\left(\frac{\nu}{\nu_0}\right)^\beta B_\nu(T).$$

Since we do not know the temperature and the mass of each clump for certain based on only the continuum emission, we will obtain a curve for each clump. Our idea is to try and search for a classification, or perhaps new constraints for the mass and temperature of these clumps in IRDCs.

Dylan Gayer would like to thank Dr. Zulema Abraham for her collaboration on the VLA proposal, as well as NSF and NRAO for making this REU opportunity possible. Dylan Gayer also extends a special thanks to Dr. Pedro Beaklini for his hard work, guidance, and support throughout this work; this work could not have been done without him.

REFERENCES

Battersby C., Ginsburg A., Bally J., Longmore S., Dunham M., Darling J., 2014, ApJ, 787, 113

Beaklini P.P.B., Mendoza E., Canelo C.M., Aleman I., Merello M., Kong S., Navarete F., et al., 2020, MNRAS, 491, 427

Bonnell, I.A., Bate, M.R., Clarke, C.J., Pringle, J.E., 1997, MNRAS, 285, 201

Bonnell I.A., Bate M.R., Clarke C.J., Pringle J.E., 2001, MNRAS, 323, 785

Butler M.J., Tan J.C., 2009, ApJ, 696, 1

de Wit W.J., Testi L., Palla F., Zinnecker H., 2005, A&A, 437, 247

Elia D., Schisano E., Molinari S., Robitaille T., Anglés-Alcázar D., Bally J., Battersby C., et al., 2010, A&A, 518, L97

Kong S., Tan J.C., Caselli P., Fontani F., Liu M., Butler M.J., 2017, ApJ, 834, 193

Li S., Sanhueza P., Zhang Q., Nakamura F., Lu X., Wang J., et al., 2020, ApJ, 903, 119

Liu J., Zhang Q., Qiu K., Liu H.B., Pillai T., et al., 2020, ApJ, 895, 142

Liu M., Tan J.C., Marvil J., Kong S., Rosero V., Caselli P., Cosentino G., 2021, arXiv:2010.11294

McKee C.F., Tan J.C., 2003, ApJ, 585, 2

Preibisch Th., Ossenkopf V., Henning Th., 1993, A&A, 279

Purser S.J.D., Lumsden S.L., Hoare M.G., Kurtz S., 2021, MNRAS, 504, 1

Tan J.C., Kong S., Butler M.J., Caselli P., Fontani F., 2013, ApJ, 779, 96